Synthetic Metals 210 (2015) 357–362

Contents lists available at ScienceDirect

Synthetic Metals

journal homepage: www.elsevier.com/locate/synmet

Sulfur-enriched, hierarchically nanoporous carbonaceous materials for sodium-ion storage

Young Soo Yun, Min Yeong Song, Na Rae Kim, Hyoung-Joon Jin*

Department of Polymer Science and Engineering, Inha University, Incheon 402-751, Republic of Korea

ARTICLE INFO

Article history:
Received 7 September 2015
Received in revised form 27 October 2015
Accepted 30 October 2015
Available online 12 November 2015

Keywords:
Porous carbon
Activated carbon
Sulfur doping
Sodium-ion
Energy storage
Carbonization

ABSTRACT

Na-ion batteries (NIBs) have had much attention as post Li-ion batteries (LIBs) due to abundant Na resources and a similar chemistry to LIBs; however NIBs have suffered from a lack of proper anode materials. In this study, sulfur-enriched, hierarchically nanoporous carbonaceous materials (SH-NCMs) were fabricated by an inclusion complex of cellulose hosted by urea hydrate through simple pyrolysis and heating with elemental sulfur. SH-NCMs had unique materials characteristics, such as a large amount of heteroatoms, containing 21.7 at.% sulfur, 12.6 at.% oxygen and 5.7 at.% nitrogen, and a 3D-interconnected mesostructure with a high surface area of 201 $m^2 g^{-1}$. Interestingly, SH-NCMs showed a high specific capacity of 456 mAh g^{-1} at a current density of 1 A g^{-1}, and even after 50 cycles at 10 A g^{-1}, a specific capacity of 170 mAh g^{-1} was achieved. In addition, stability over more than 500 repetitive cycles with nearly 100% Coulombic efficiency was maintained.

1. Introduction

Li-ion batteries (LIBs) are one of the most reliable energy storage systems [1,2]. However, Li resources are insufficient and their reserves are located in remote or politically sensitive areas [3,4]. As an alternative to LIBs, a feasible post-LIB are Na-ion batteries (NIBs), due to abundant supplies and widespread terrestrial reserves of Na resources as well as a similar chemistry to LIBs [3,4]. In the chemistry of NIBs, the primary hurdle of a proper anode material for Na-ion storage is absent because Na-ions cannot be intercalated in graphite, one of the best anode materials which led to the commercial success of LIBs [5]. Therefore, various alternative anode materials have been studied for NIBs, such as hard carbons, [6,7] metal oxides, [8,9] phosphides [10] and phosphorous [11,12]. However, these anode materials have limitations in terms of poor rate performance, cyclic stability, high-cost and/or complex synthetic processes. In contrast, nanostructured carbonaceous materials (NCMs) have shown great rate performances and cyclic stabilities by pseudocapacitive Na-ion storage behavior [13–19]. Tang et al. reported hollow carbon nanospheres with superior rate capabilities in which a specific capacity of approximately 50 mAh g^{-1} was achieved at a current rate of 10 A g^{-1} [13]. Wang et al. showed that carbon nanofibers have a reversible capacity of 73 mAh g^{-1} at a current density of 20 A g^{-1} and good cyclic stabilities over 200 cycles [14]. Additionally, various types of carbon nanofibers [15,16]. and carbon nanosheets [17,18] have been designed as anode materials for NIBs. The Na-ion storage performance on NCMs is highly dependent on their nanostructure and surface properties because the pseudocapacitive charge storage primarily happens on the surface and/or near the surface of the electrode materials. Therefore, a more advanced design, such as numerous redox active heteroatoms, could result in a dramatic enhancement of the electrochemical performances for sodium-ion storage.

In this study, hierarchically nanoporous carbonaceous materials containing numerous sulfur atoms (SH-NCMs) were fabricated from an inclusion complex (IC) of cellulose hosted by urea hydrate using pyrolysis and heating with elemental sulfur. The SH-NCMs exhibited unique material properties, leading to notable electrochemical performances as an electrode material for Na-ion storage. This study provides effects of sulfur atoms on nanostructured carbonaceous electrodes for Na-ion storage.

2. Methods

2.1. Preparation of SH-NCMs

Hierarchically nanoporous carbonaceous materials (H-NCMs) were prepared using a previously reported procedure [20,21]. A mixture of a 7 wt.% NaOH/12 wt.% urea/81 wt.% water solution pre-

* Corresponding author. Fax.: +82 32 865 5178.
E-mail address: hjjin@inha.ac.kr (H.-J. Jin).

http://dx.doi.org/10.1016/j.synthmet.2015.10.025
0379-6779/

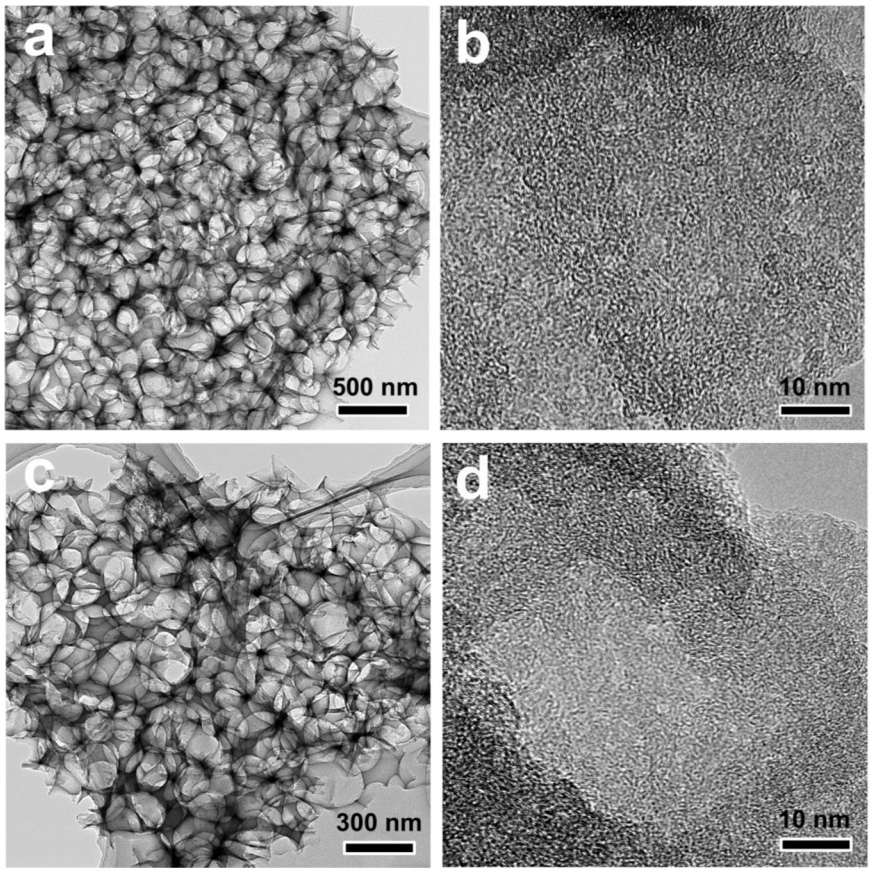

Fig. 1. FE-TEM images of (a), (b) SH-NCMs and (c), (d) H-NCMs.

cooled to −12 °C for 2 h was prepared, and 5 wt.% cotton cellulose (Aldrich) was immersed in the mixture solution, which was then intensely stirred for approximately 5 min at ambient temperature (IC solution). The IC solutions were then frozen at −196 °C and then freeze-dried for three days. The IC cryogel was carbonized starting at room temperature to 600 °C for 1 h. A heating rate of 10 °C min^{-1} and an Ar flow of 200 mL min^{-1} were applied. After the cryogel was carbonized, it was washed using distilled water and ethanol and then dried in a vacuum oven at 30 °C for 24 h. Next, the product materials (H-NCMs) were heated with elemental sulfur at a weight ratio of 1:1 starting at room temperature to 600 °C for 1 h. A heating rate of 10 °C min^{-1} and an Ar flow of 200 mL min^{-1} were applied. After the heat treatment, the resulting products (SH-NCMs) were washed using distilled water and ethanol, and then stored in a vacuum oven at 30 °C.

2.2. Characterization

The morphologies of the samples were observed by field emission transmission electron microscopy (FE-TEM; JEM2100F, JEOL, Japan). XRD (Rigaku DMAX 2500) analysis was performed using Cu Kα radiation (wavelength λ = 0.154 nm) operated at 40 kV and 100 mA. The porous properties of the samples were characterized using nitrogen adsorption and desorption isotherms, which were obtained using a surface area and porosimetry analyzer (ASAP 2020, Micromeritics, USA) at −196 °C. X-ray photoelectron spectroscopic analysis (XPS, PHI 5700 ESCA) was performed using monochromated Al Kα radiation ($h\nu$ = 1486.6 eV). A four-probe method with an electrical conductivity meter (Loresta GP, Mitsubishi Chemical, Japan) was used to measure the electrical conductivity of the samples.

2.3. Electrochemical characterization

The electrochemical properties of the SH-NCMs were characterized using a Wonatec automatic battery cycler and CR2032-type coin cells. The coin cells were assembled in a glove box filled with argon using SH-NCMs as the working electrode and metallic Na

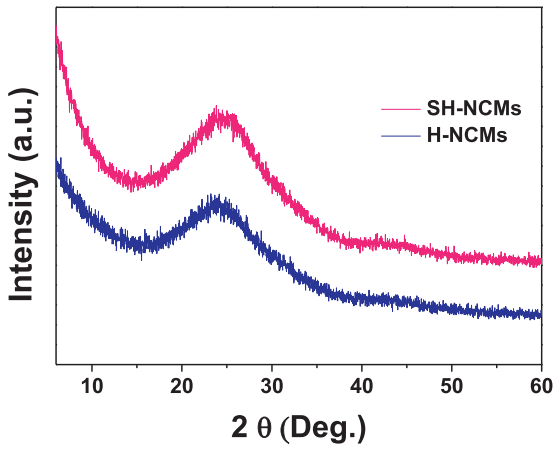

Fig. 2. XRD patterns of SH-NCMs and H-NCMs.

Table 1
Textural properties, and carbon, oxygen, nitrogen and sulfur contents of the H-NCMs and SH-NCMs.

Sample name	S_{BET} ($m^2 g^{-1}$)	S_{MIC} ($m^2 g^{-1}$)	S_{MESO} ($m^2 g^{-1}$)	Carbon (at.%)	Oxygen (at.%)	Nitrogen (at.%)	Sulfur (at.%)
H-NCMs	492	230	262	72.9	17.6	9.5	–
SH-NCMs	201	103	98	45.0	12.6	5.7	21.7

foils as both the reference and counter electrodes. 1 M $NaClO_4$ (1 M; Aldrich, purity: 99.99%) was dissolved in a solution of ethylene carbonate (EC) and propylene carbonate (PC) (1:1 v/v) and used as the electrolyte for Na-ion storage. A glass microfiber filter separator (GF/F, Whatman) was used as the separator. The working electrodes were prepared by mixing the active material (70 wt.%) with conductive carbon (20 wt.%) and polyvinylidene fluoride (10 wt.%) in *N*-methyl-2-pyrrolidone. The resulting slurries were uniformly applied to the Al foil. The electrodes were dried at 120 °C for 2 h and roll pressed. The mass loading of the active materials was approximately 1 mg cm^{-2} and the total electrode weight was approximately 2–3 mg. The cells were galvanostatically cycled between 0.005 and 2.5 V at various currents. Electrochemical impedance spectroscopy (EIS, VSP-300, Bio-Logic, France) measurements were performed from 3 MHz to 100 mHz.

3. Results and discussion

The morphologies of the SH-NCMs and H-NCMs were observed by FE-TEM as shown in Fig. 1. The three-dimensionally interconnected macroporous structure was confirmed and the macropore size was approximately 150 nm (Fig. 1(a)). Additionally, the high-resolution TEM images show that the SH-NCMs have an amorphous carbon structure without long range ordering of the graphitic structure. The morphology and microstructure are similar to that of H-NCMs (Fig. 1(c) and (d)), which indicated that the thermal treatment of H-NCMs with elemental sulfur slightly affected their morphology and the local carbon ordering. The XRD data supports that the SH-NCMs and H-NCMs have an amorphous carbon structure (Fig. 2). In the XRD pattern of SH-NCMs, only a very broad graphite (0 0 2) peak was observed; this indicated a poor stacking of hexagonal carbon

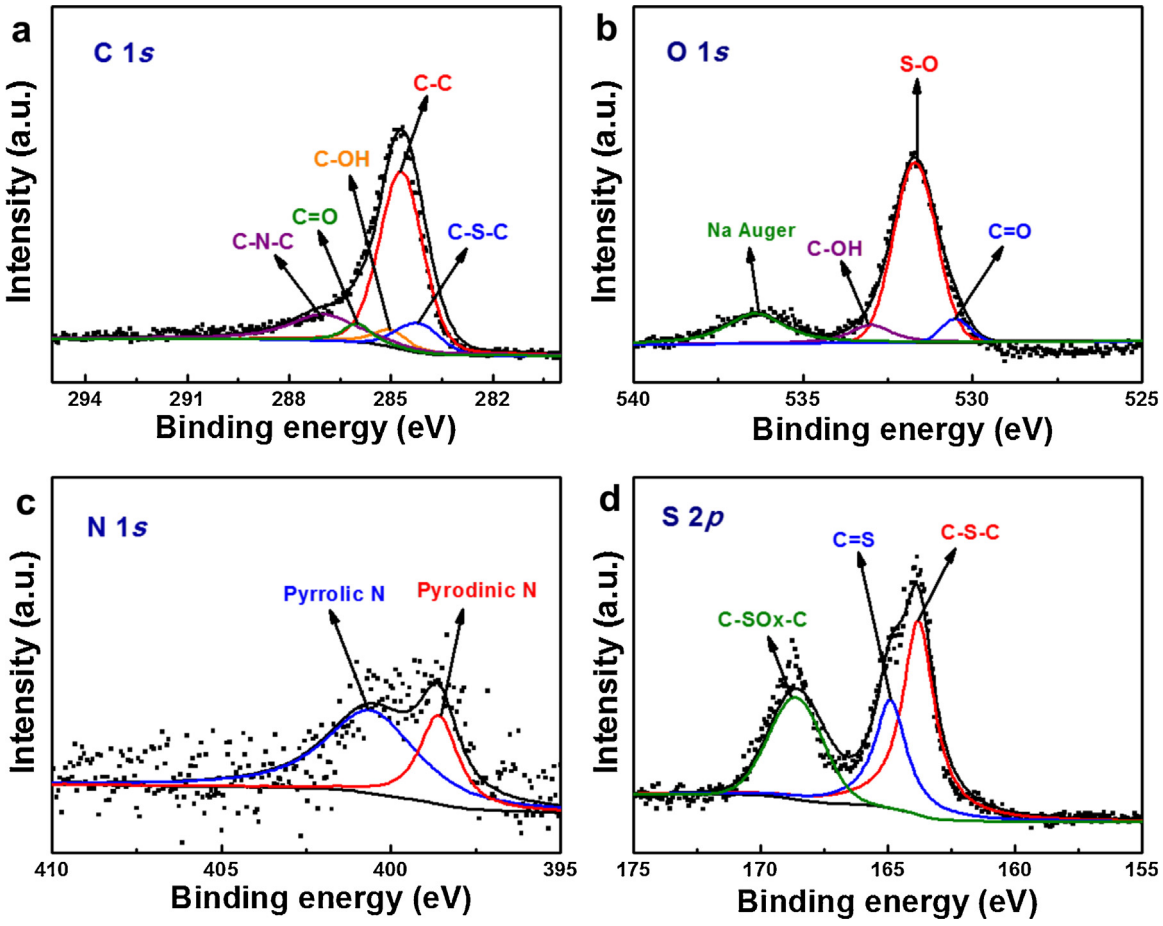

Fig. 3. XPS (a) C 1s, (b) O 1s, (c) N 1s and (d) S 2p spectra of SH-CNSs.

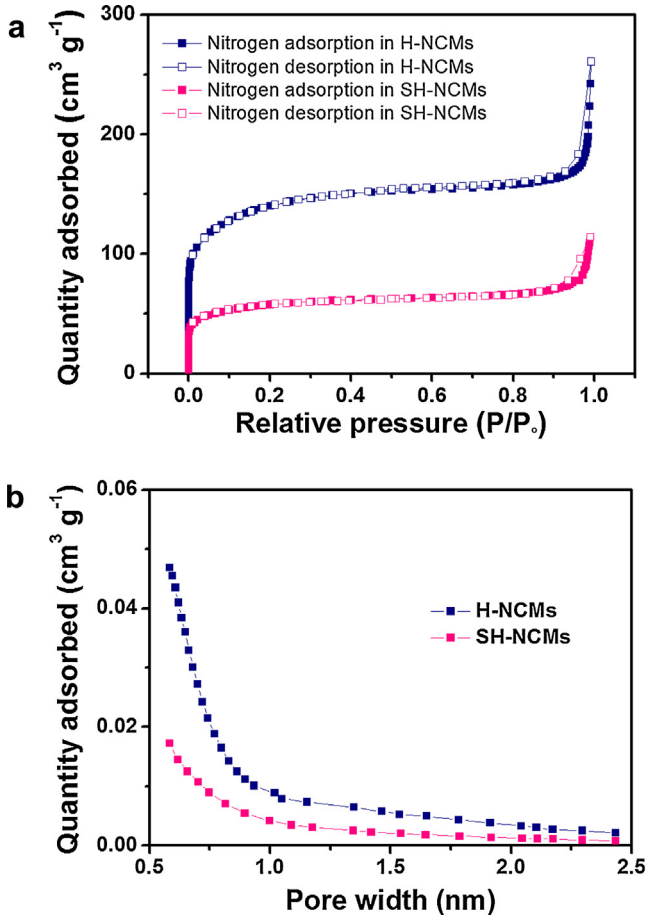

Fig. 4. (a) Nitrogen adsorption and desorption isotherm curves and (b) pore-size distributions of SH-NCMs and H-NCMs.

layers, which have a highly defective hexagonal carbon structure [22], because the pyrolysis at 600 °C and annealing at 600 °C were insufficient in forming hexagonal carbon structures and their stacking. Additionally, the heteroatoms of the precursor material could not be fully removed at this temperature, suggesting that heteroatom-enriched carbonaceous materials can be fabricated.

Table 1 shows the contents of heteroatoms in H-NCMs and SH-NCMs. H-NCMs contain numerous oxygen and nitrogen atoms, which correspond to C/O and C/N ratios of 4.14 and 6.94, respectively. After heating with elemental sulfur, the relative oxygen and nitrogen contents decreased and numerous sulfur atoms of 21.7 at.% were introduced at the surface of the H-NCMs. The C/O, C/N and C/S ratios of SH-NCMs were 4.39, 10.53 and 2.76. Note that the C/O ratio slightly increased after thermal treatment with elemental sulfur, while the C/N ratio increased relatively significantly, which indicated that the oxygen atoms were slightly removed even though a large amount of nitrogen atoms were released after heating. In addition, numerous sulfur atoms were doped on the surface of the H-NCMs (Table 1). The specific chemical bonding nature of SH-NCMs are exhibited in Fig. 3. In the XPS C 1s spectrum of SH-NCMs, several peaks, such as C—S—C, C—OH, C=O and C—N—C bondings centered at 284.3, 285.0, 286.0 and 287.0 eV, respectively, were observed, including the main CC bonding centered at 284.7 eV (Fig. 3(a)). Additionally, in the O 1s spectrum, the main S—O bonding centered at 531.7 eV was confirmed with minor C—OH and C=O bondings centered at 533.1 and 530.5 eV, respectively (Fig. 3(b)). The Na auger centered at 536.1 eV could be induced from NaOH in the pyrolysis process. In addition, two distinct peaks such as pyridinic nitrogen and pyrrolic nitrogen centered at 398.6 and 400.6 eV, respectively, were observed in the XPS N 1s spectrum (Fig. 3(c)). The sulfur atoms were primarily introduced as forms of C—S—C, C=S and C—SO_x—C centered at 163.8, 164.9 and 168.6 eV, respectively (Fig. 3(d)) [23].

The pore characteristics were investigated by a nitrogen adsorption and desorption isotherm method, as shown in Fig. 4. The isotherm curves of H-NCMs and SH-NCMs show the IUPAC type-I and -IV hybrid shapes, indicating that both the microporous and mesoporous structures were well-developed (Fig. 4(a)). However, H-NCMs have a larger specific volume adsorbed than SH-NCMs because the heavier sulfur atoms were introduced on the surface of H-NCMs as opposed to the collapse of the porous structure of H-NCMs after heating with elemental sulfur. The pore size distribution data of H-NCMs and SH-NCMs demonstrates that their micropores were primarily less than 0.7 nm, indicating ultramicropores (Fig. 4(b)). These ultramicropores could be induced by the activation effects of NaOH. The specific surface area of the H-NCMs and SH-NCMs were 492 and 201 $m^2 g^{-1}$ and their micropore surface areas were 230 and 104 $m^2 g^{-1}$, respectively (Table 1).

The electrochemical properties of the SH-NCMs were investigated in an electrolyte of 1 M $NaClO_4$ dissolved in an EC/PC (1:1 v/v) solution in a potential range between 0.005 and 2.5 V*vs.* Na/Na^+. The reversible capacity of SH-NCMs was 456 mAh g^{-1} at a current density of 1 A g^{-1}, which was much greater than 206 mAh g^{-1} of H-NCMs (Fig. 5(a)). Additionally, most capacities (approximately 320 mAh g^{-1}) were induced between 1 and 2 V*vs.* Na/Na^+, which is distinct from the linear profile of H-NCMs (Fig. 5(a)). Cyclovoltammograms of SH-NCMs and H-NCMs showed the differences more clearly (Fig. 5(b) and (c)). In the first cycle of SH-NCMs and H-NCMs, the cyclovoltammograms showed large cathodic peaks around 0.5 V, which can be considered as solid-electrolyte-interface (SEI) layer formation reaction on the electrode surface. Also, the cyclovoltammogram of SH-NCMs showed two cathodic peaks at 1.1 V and 1.8 V and anodic peak at 1.95 V in the second cycle, indicating reversible redox reactions. In contrast, the cyclovoltammogram of H-NCMs showed no distinct redox peak in the second cycle. The differences in the specific capacity, profile and cyclovoltammogram indicate that the Na-ion storage mechanism of both electrode materials is different, which could originate from the numerous sulfur atoms on the surface of the SH-NCMs. Note that the SH-NCMs showed high rate performance despite their poor electrical conductivity (8.2×10^{-2} S cm^{-1}). After 50 cycles at current densities of 1, 2, 5, 7.5 and 10 A g^{-1}, SH-NCMs exhibited specific capacities of 317, 284, 231, 193 and 170 mAh g^{-1}, respectively (Fig. 5(d)). These values are much greater than 165, 146 and 118 mAh g^{-1} of H-NCMs at current densities of 1, 2 and 5 A g^{-1}, respectively. The high rate capabilities of SH-NCMs were further illustrated by Nyquist plots according to Na-ion insertion and extraction as shown in Fig. 5(e) and (f). The semicircles, which mean the faradic charge transfer resistance, and Warburg diffusion resistances gradually decreased with Na-ion insertion. The equivalent series resistance (ESR) was approximately 780 Ω in the pristine SH-NCMs-based electrodes without Na-ion insertion, and after Na-ion was fully inserted, it reached approximately 290 Ω (Fig. 5(e)). In contrast, as the Na-ion was extracted, the ESR of the SH-NCMs-based electrodes increased reversibly, and returned to their initial value (Fig. 5(f)). These results can be attributed to the doping effects of the Na-ion on the carbonaceous structure, which could increase the electrical transport properties of the SH-NCMs. The current density*vs.* capacity plot is exhibited in Fig. 6(a) [13–18,24]. The specific capacities of SH-NCMs were

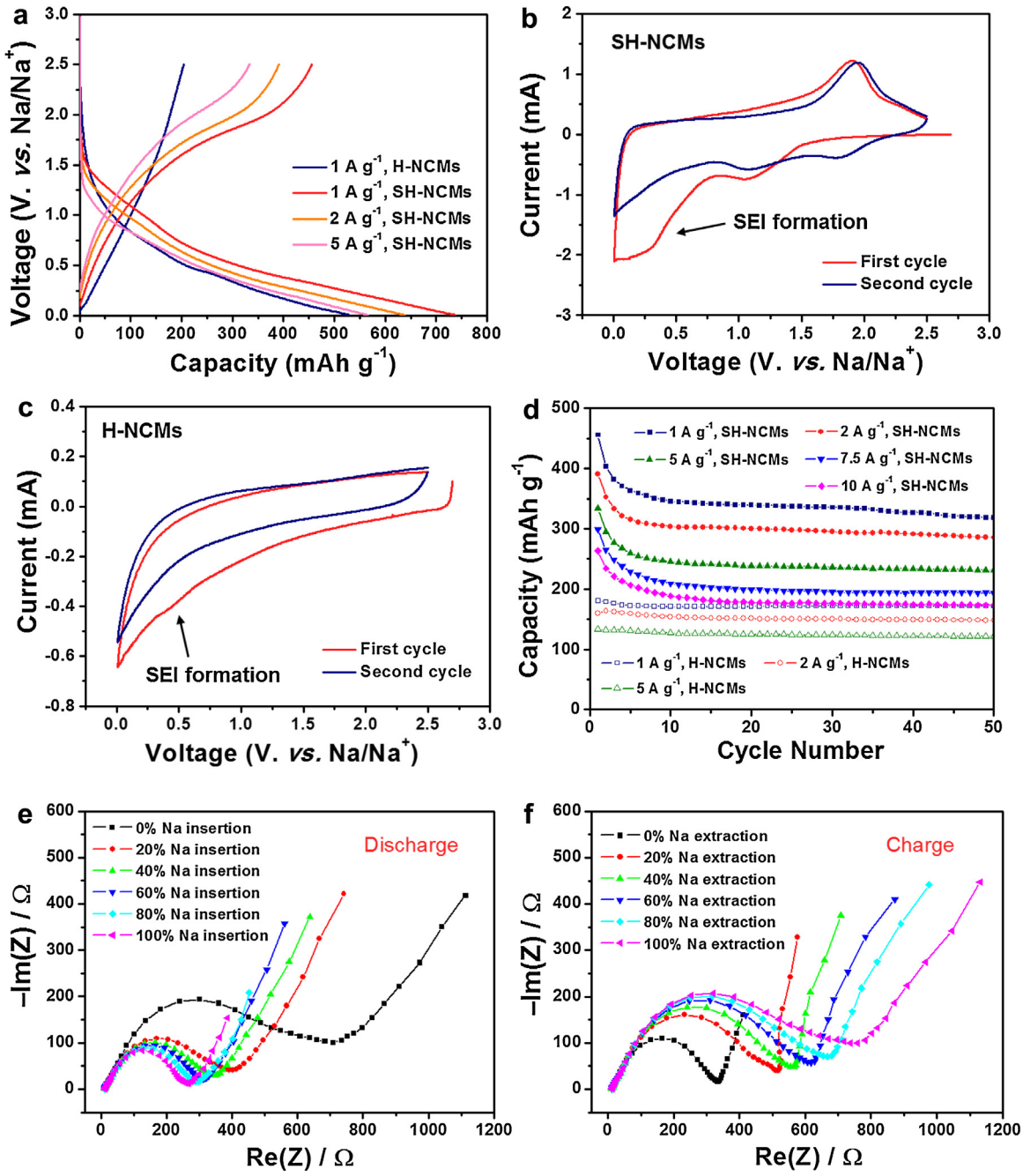

Fig. 5. (a) Galvanostatic discharge/charge profiles of SH-NCMs and H-NCMs for Na-ion storage at current densities of 100, 200 and 500 mA g^{-1} for SH-NCMs and 100 mA g^{-1} for H-NCMs in a voltage range of 0.005–2.5 V *vs.* Na/Na^+. Cyclovoltammograms of (b) SH-NCMs and (c) H-NCMs at a scan rate of 1 mV s^{-1}. (d) Rate capabilities and cyclic stabilities over 50 cycles of SH-NCMs and H-NCMs for Na-ion storage at a current density of 100, 200, 500, 750 and 1000 mA g^{-1} for SH-NCMs and 100, 200 and 500 mAh g^{-1}. Nyquist plots of SH-NCMs according to Na (e) insertion and (f) extraction.

superior to the reported values in the given current densities from 1 to 10 A g^{-1}. In addition, SH-NCMs showed stable cycles over consecutive 1000 cycles with a Coulombic efficiency of nearly 100% (Fig. 6(b)).

4. Conclusion

SH-NCMs were fabricated from an IC of cellulose hosted by urea hydrate using pyrolysis and heating with elemental sulfur. The SH-NCMs had a 3D-interconnected porous structure with a specific surface area of 201 $m^2 g^{-1}$, and numerous heteroatoms such as 21.7 at.% sulfur, 12.6 at.% oxygen and 5.7 at.% nitrogen. The sulfur atoms induced a significant enhancement of the specific capacity in a potential range between 1 and 2 V *vs.* Na/Na^+. Additionally, despite the poor electrical conductivity of SH-NCMs (8.2×10^{-2} S cm^{-1}), they showed good rate capabilities in which the specific capacity of 170 mAh g^{-1} was achieved at a high current density of 10 A g^{-1}. In addition, SH-NCMs showed stable cycles over 1000 cycles.

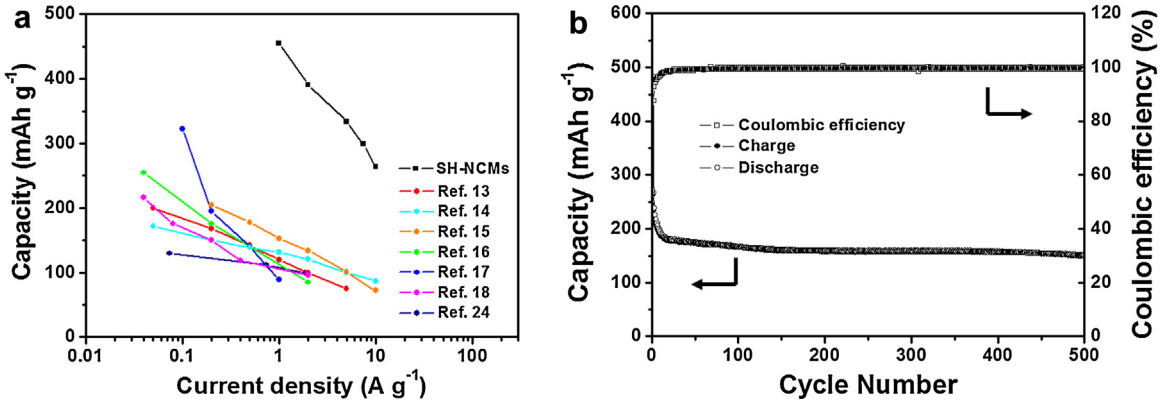

Fig. 6. (a) Current density *vs.* capacity plots of various anode materials for NIBs [13–18,24]. (b) Cyclic performance of SH-NCMs over 500 repetitive cycles and Coulombic efficiency.

References

[1] J.-M. Tarascon, M. Armand, Nature 414 (2001) 359–367.
[2] V. Etacheri, R. Marom, R. Elazari, G. salitra, D. Aurbach, Energy Environ. Sci. 4 (2011) 3243–3262.
[3] S.-W. Kim, D.-H. Seo, X. Ma, G. Ceder, K. Kang, Adv. Energy Mater. 2 (2012) 710–721.
[4] H. Kim, J. Hong, Y.-U. Park, J. Kim, I. Hwang, K. Kang, Adv. Funct. Mater. 25 (2015) 534–541.
[5] D.A. Stevens, J.R. Dahn, J. Electrochem. Soc. 148 (2001) A803–A811.
[6] D.A. Stevens, J.R. Dahn, J. Electrochem. Soc. 147 (2000) 1271–1273.
[7] S. Komaba, W. Murata, T. Ishikawa, N. Yabuuchi, T. Ozeki, T. Nakayama, A. Ogata, K. Gotoh, K. Fujiwara, Adv. Funct. Mater. 21 (2011) 3859–3867.
[8] B. Koo, S. Chattopadhyay, T. Shibata, V.B. Prakapenka, C.S. Johnson, T. Rajh, E.V. Shevchenko, Chem. Mater. 25 (2013) 245–252.
[9] Y. Sun, L. Zhao, H. Pan, X. Lu, Y.-S. Hu, H. Li, M. Armand, Y. Ikuhara, L. Chen, X. Huang, Nat. Commun. 4 (2013) 1870.
[10] Y. Kim, Y. Kim, A. Choi, S. Woo, D. Mok, N.-S. Choi, Y.S. Jung, J.H. Ryu, S.M. Oh, K. T. Lee, Adv. Mater. 26 (2014) 4139–4144.
[11] Y. Kim, Y. Park, A. Choi, N.-S. Choi, J. Kim, J. Lee, J.H. Ryu, S.M. Oh, K.T. Lee, Adv. Mater. 25 (2013) 3045–3049.
[12] J. Qian, X. Wu, Y. Cao, X. Ai, H. Yang, Angew. Chem. 52 (2013) 4633–4636.
[13] K. Tang, L. Fu, R.J. White, L. Yu, M.-M. Titirici, M. Antonietti, J. Maier, Adv. Energy Mater. 2 (2012) 873–877.
[14] Z. Wang, L. Qie, L. Yuan, W. Zhang, X. Hu, Y. Huang, Carbon 55 (2013) 328–334.
[15] L. Fu, K. Tang, K. Song, P.A. van Aken, Y. Yu, J. Maier, Nanoscale 6 (2014) 1384–1389.
[16] W. Luo, J. Schardt, C. Bommier, B. Wang, J. Razink, J. Simonsen, X. Ji, J. Mater. Chem. A 1 (2013) 10662–10666.
[17] H.-G. Wang, Z. Wu, F.-L. Meng, D.-L. Ma, X.-L. Huang, L.-M. Wang, X.-B. Zhang, ChemSusChem 6 (2013) 56–60.
[18] Y.-X. Wang, S.-L. Chou, H.-K. Liu, S.X. Dou, Carbon 57 (2013) 202–208.
[19] Y.S. Yun, S.Y. Cho, H. Kim, H.-J. Jin, K. Kang, ChemElectroChem 2 (2015) 359–365.
[20] Y.S. Yun, J. Shim, Y. Tak, H.-J. Jin, RSC Adv. 2 (2012) 4353–4358.
[21] Y.S. Yun, D. Kim, H.H. Park, Y. Yak, H.-J. Jin, Synth. Met. 162 (2012) 2337–2341.
[22] S.Y. Cho, Y.S. Yun, S. Lee, D. Jang, K.-Y. Park, J.K. Kim, B.H. Kim, K. Kang, D.L. Kaplan, H.-J. Jin, Nat. Commun. 6 (2015) 7145.
[23] Y.S. Yun, V.-D. Le, H. Kim, S.-J. Chang, S.J. Baek, S. Park, B.H. Kim, Y.-H. Kim, Y.-H. Kim, K. Kang, H.-J. Jin, J. Power Sources 262 (2014) 79–85.
[24] S. Wenzel, T. Hara, J. Janek, P. Adelhelm, Energy Environ. Sci. 4 (2011) 3342–3345.